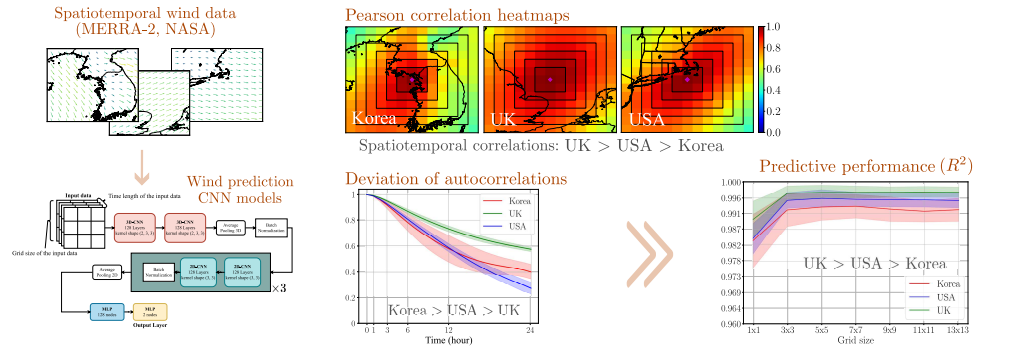


# Graphical Abstract

## Effects of spatiotemporal correlations in wind data on neural network-based wind predictions

Heesoo Shin, Mario Rüttgers, Sangseung Lee

Effects of spatiotemporal correlations in wind data on neural network-based wind prediction



Heesoo Shin, Mario Rüttgers and Sangseung Lee (2023)

“Regional wind characteristics influence the learnability of CNNs”

Energy

## Highlights

### **Effects of spatiotemporal correlations in wind data on neural network-based wind predictions**

Heesoo Shin, Mario Rüttgers, Sangseung Lee

- 3D CNN-based wind velocity prediction.
- Estimation of CNN learnability through spatiotemporal wind correlation analysis.
- Discovery of influence of local geometric and seasonal wind on CNN prediction.
- The proposed correlation analysis can aid in selecting yaw-control wind farm sites.

# Effects of spatiotemporal correlations in wind data on neural network-based wind predictions

Heesoo Shin<sup>a</sup>, Mario Rüttgers<sup>b,c,d</sup>, Sangseung Lee<sup>a,\*</sup>

<sup>a</sup>*Department of Mechanical Engineering, Inha University Incheon, 22212, Republic of Korea*

<sup>b</sup>*Institute of Aerodynamics and Chair of Fluid Mechanics (AIA), RWTH Aachen University Aachen, 52062, Germany*

<sup>c</sup>*Jülich Supercomputing Centre (JSC), Forschungszentrum Jülich GmbH, Jülich, 52425, Germany*

<sup>d</sup>*Jülich Aachen Research Alliance - Center for Simulation and Data Science (JARA-CSD), Aachen, 52074, Germany*

---

## Abstract

This paper investigates the influence of incorporating spatiotemporal wind data on the performance of wind forecasting neural networks. While previous studies have shown that including spatial data enhances the accuracy of such models, limited research has explored the impact of different spatial and temporal scales of input wind data on the learnability of neural network models. In this study, convolutional neural networks (CNNs) are employed and trained using various scales of spatiotemporal wind data. The research demonstrates that using spatiotemporally correlated data from the surrounding area and past time steps for training a CNN favorably affects the predictive performance of the model. The study proposes correlation analyses, including autocorrelation and Pearson correlation analyses, to unveil the influence of spatiotemporal wind characteristics on the predictive performance of different CNN models. The spatiotemporal correlations and performances of CNN models are investigated in three regions: Korea, the USA, and the UK. The findings reveal that regions with smaller deviations of autocorrelation coefficients (ACC) are more favorable for CNNs to learn the regional and seasonal wind characteristics. Specifically, the regions of Korea, the USA, and the UK exhibit maximum standard deviations of ACCs of 0.100, 0.043, and 0.023, respectively. The CNNs wind prediction performances follow the reverse order of the regions: UK, USA, and Korea. This highlights the significant impact of regional and seasonal wind conditions on the performance of the prediction models.

*Keywords:*

Spatiotemporal data, Artificial neural network, Autocorrelation, Pearson correlation coefficient, 3D-Convolutional neural networks

---

## 1 Introduction

With rising concerns regarding global warming and energy security, there is an increasing demand for renewable energy sources, such as wind energy [1]. Wind turbines convert the kinetic energy of atmospheric flow into electrical energy. The maximum power generation of wind turbines depends significantly on the alignment of the turbine nacelle with the surrounding flow [2, 3]. Yaw control systems have been proposed to align wind turbines with the wind direction [4, 5, 6]. One of the most common methods is to use sensors installed at the rear of the turbine to align the turbine with the wind direction. However, the wake effect caused by the rotating blades can lead to deviations in the wind velocity measured by sensors from the actual wind speed [5]. Therefore, accurately predicting the wind direction remains a significant challenge. Researchers are investigating methods for accurately predicting the wind direction to enable effective yaw control.

Recently, neural networks have shown promising results in addressing atmospheric flow problems, such as typhoon prediction [7, 8]. Neural-network-based wind predictions have also been investigated by various researchers [9, 10, 11]. These studies primarily involved the training of neural networks using wind data from a single point. Although wind turbines are installed at specific locations, the wind itself is not a localized phenomenon. This is influenced by macroscopic systems and global parameters. In a study by Hong and Satriani [12], spatiotemporal wind data were utilized in a 2D-Convolutional neural network (CNN) model to predict wind at a specific location. The training data were sourced from multiple locations, including nearby wind farms in close proximity. The 2D-CNN model outperformed long short-term memory (LSTM) and 1D-CNN models that used data from only one wind farm, demonstrating the importance of utilizing spatiotemporal data for wind prediction.

---

\*Coressponding author

*Email addresses:* [hs\\_Shin@inha.edu](mailto:hs_Shin@inha.edu) (Heesoo Shin ),  
[m.ruettgers@aia.rwth-aachen.de](mailto:m.ruettgers@aia.rwth-aachen.de) (Mario Rüttgers ), [sanseunglee@inha.ac.kr](mailto:sanseunglee@inha.ac.kr)  
(Sangseung Lee )

*Preprint submitted to Energy*

*June 21, 2023*

29 In a study by Higashiyama et al. [13], the impact of surrounding spatial  
30 data on wind power generation was investigated. The dataset used in the  
31 study consisted of numerical weather data collected from  $50 \times 50 = 2,500$   
32 points surrounding a single targeted wind power plant in the Tohoku region  
33 with a time resolution of 30 minutes and regular horizontal spacing of 5  
34 km. A 3D-CNN model was employed to analyze the spatiotemporal data,  
35 which is capable of learning spatial and temporal features concurrently. The  
36 results of this study showed that the 3D-CNN model outperformed the 2D-  
37 CNN model. In addition, Zhu et al. [14] utilized a Fully 3D-CNN model  
38 to predict wind speed using wind data collected from 36 individual wind  
39 turbines on a wind farm located in China with a time interval of one day.  
40 Because the turbines are located in close proximity to one another, the data  
41 collected by each turbine can be considered spatially correlated. Their Fully  
42 3D-CNN model was reported to have superior performance compared to two  
43 statistical models (the persistence (PR) method and vector autoregression  
44 (VAR)) and three neural networks (LSTM, CNN-LSTM, and CNN-gate  
45 recurrent unit (GRU)).

46 Previous studies have demonstrated that the incorporation of spatial  
47 data can improve the accuracy of wind prediction models. However, not  
48 enough research has been conducted on the physical mechanisms underlying  
49 this improvement, as well as the effect of time intervals on input data in such  
50 models. Therefore, this study aims to address these gaps by investigating  
51 the impact of spatiotemporal wind data on CNN-based wind predictions.  
52 The objective is to elucidate the influence of regional and seasonal wind  
53 flow factors on the learning capabilities of CNNs. In particular, the role of  
54 spatiotemporal wind data in enhancing the performance of CNN models for  
55 wind prediction is analyzed. This study examines the effect of varying the  
56 input spatial area and time intervals on the model’s predictive capabilities  
57 and investigates the influence of regional and seasonal wind flow patterns  
58 on predictive performances in different types of CNN models.

59 The remainder of this paper is organized as follows. In Section 2, a  
60 detailed description of the utilized wind data is provided, including the pro-  
61 cessing steps required to transform the data into a suitable form for a CNN.  
62 Section 3 outlines the methodological approach used to adjust the wind data  
63 to a wind turbine’s height (Section 3.1) and describes the proposed CNN’s  
64 architecture, which is a combination of 2D and 3D CNNs, and training  
65 process (Section 3.2). In Section 4, the performance of the proposed CNN  
66 model under varying spatiotemporal input data is analyzed, and the sea-

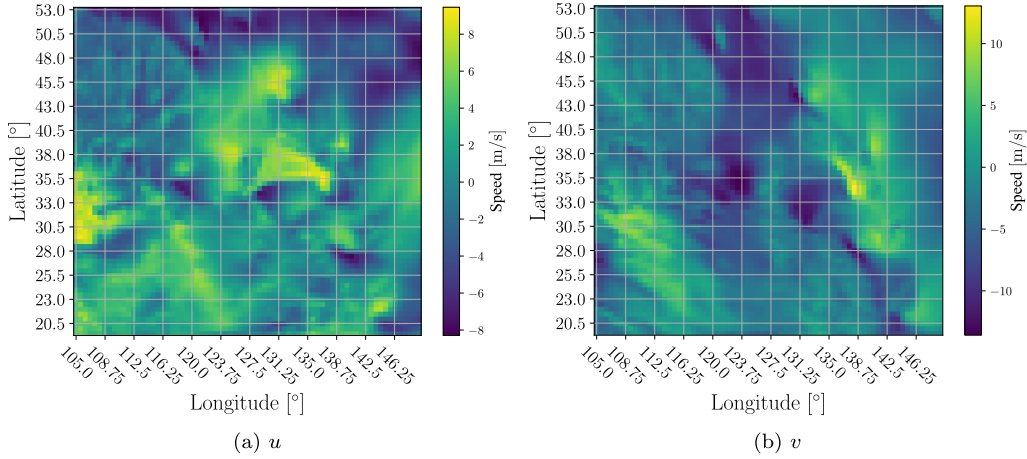


Figure 1:  $u$  and  $v$  components of wind velocity at an altitude of 50 m in South Korea on January 1, 2012 at 00:00.

67 sonal and regional factors that influence the network’s predictive capability  
 68 are highlighted. In addition, the proposed model was compared with CNN  
 69 models from other studies. Finally, Section 5 summarizes the key findings.

## 70 2. Data description

71 This study utilizes the Modern-Era Retrospective Analysis for Research  
 72 and Applications version 2 (MERRA-2) dataset provided by the National  
 73 Aeronautics and Space Administration (NASA)[15]. The dataset has a time  
 74 interval of one hour with hourly averaged values. It was rearranged in a grid  
 75 format in which each grid point was assigned to the corresponding latitude  
 76 and longitude coordinates. The grid was constructed at constant intervals  
 77 in each latitudinal and longitudinal direction, forming a rectangular grid  
 78 structure (refer to Figure 1).

79 The wind data are composed of the east-west wind speed ( $u$ ) and north-  
 80 south wind speed ( $v$ ), at an altitude of 50 m. They cover the Korean  
 81 Peninsula and surrounding areas, the UK and surrounding areas, and the  
 82 northeastern USA, which allowed for a comparative analysis of the pre-  
 83 diction performance across different regions (see Figure 2). Moreover, the  
 84 study focused on predicting wind power generation at individual points  
 85 corresponding to real-world wind farms in the UK and USA, as well as one  
 86 candidate site for a future wind farm in Korea. The spatial information of  
 87 each dataset and the prediction points can be found in Table 1.

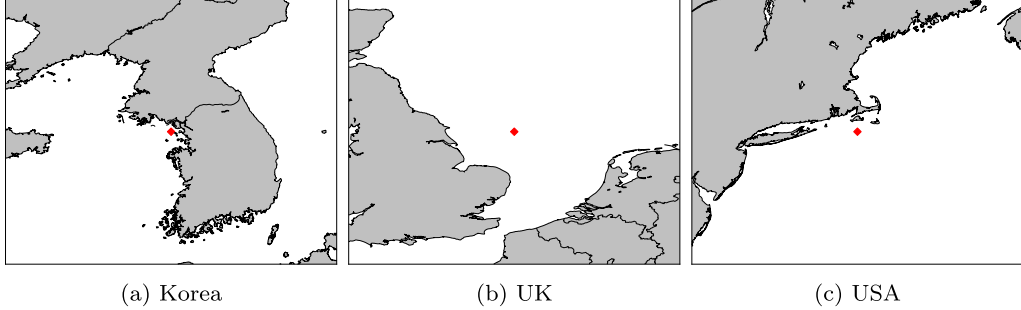


Figure 2: Maps with the three different prediction points and their surrounding area. The prediction points are represented by the red mark.

Location	Lat. UL	Lat. LL	Lon. UL	Lon. LL	Prediction point
Korea	54.0° N	20.5° N	149.4° E	105.0° E	37.5° N 126.3° E
UK	68.5° N	39.5° N	16.3° E	21.9° W	54.0° N 1.9° E
USA	49.0° N	35.0° N	63.8° W	79.4° W	41° N 70.6° W

Table 1: Spatial information of the datasets. UL and LL denote the upper and lower limits, respectively.

88 The 3D-CNN was trained and tested using a 10-year period of data from  
 89 January 1, 2012 to January 1, 2022. The dataset was partitioned into  
 90 three subsets: 60% of the data were used for training (from January 1,  
 91 2012 to January 1, 2018), 20% for validation (from January 2, 2018 to  
 92 January 1, 2020), and the remaining 20% for testing (from January 2,  
 93 2020 to January 1, 2022).

94 The impact of the surrounding information on wind prediction was in-  
 95 vestigated by incrementally increasing the latitude and longitude by  $\Delta_{latitude}$   
 96  $= 0.5^\circ$  and  $\Delta_{longitude} = 0.625^\circ$ , respectively. The examined area began with  
 97 a  $3 \times 3$  grid and gradually increased to a  $13 \times 13$  grid (refer to Figure 3).

98 In the experiments, the effects of different time periods on wind flow  
 99 prediction were studied. Specifically, time lengths of  $T = 3, 6, 12, 24$  h were  
 100 considered. The CNN model used past wind data with a time interval of one  
 101 hour to predict the wind flow for the upcoming hour. For example, when  
 102  $T = 6$ , six consecutive snapshots of wind data obtained between January  
 103 1, 2022, 06:00 and January 1, 2022, 11:00 were used to forecast  $u$   
 104 and  $v$  values at January 1, 2022, 12:00.

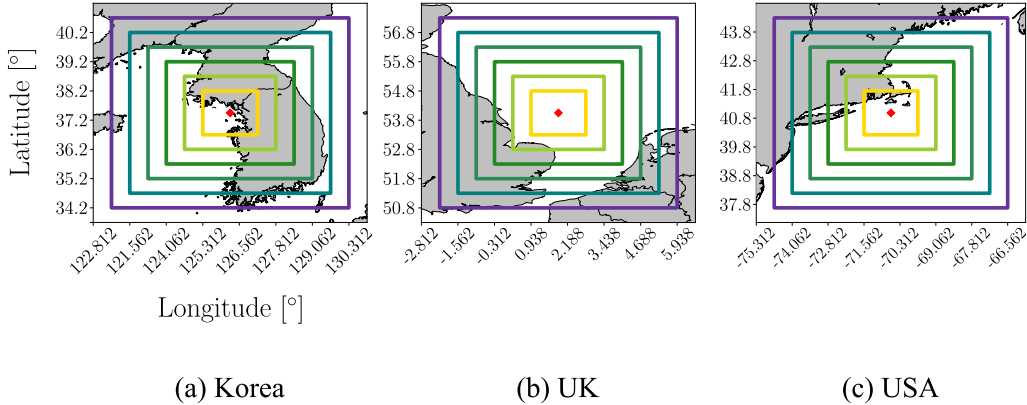


Figure 3: Visualization of the grid sizes in the three different regions.

### 105 3. Methodology

106 The methodology section explains the details of the employed (1) Atmo-  
 107 spheric boundary layer (ABL) calibration and (2) Neural network model.  
 108 The first subsection focuses on the ABL calibration method, which is em-  
 109 ployed to adapt the original wind data to the height of typical wind tur-  
 110 bines. The architecture and hyperparameters of the employed 2D+3D-  
 111 Convolutional Neural Network (2D+3D-CNN) model are explained in the  
 112 second subsection.

#### 113 3.1. Atmospheric boundary layer calibration

114 The wind data available from the MERRA-2 dataset were collected at  
 115 a height of 50m. However, it is possible to approximate the wind velocity  
 116 at different heights from the MERRA-2 dataset using the ABL calibration.  
 117 This is particularly helpful when studying wind at heights where wind tur-  
 118 bines are typically installed (e.g., 100m).

119 The ABL estimates wind speed and direction at different heights by  
 120 accounting for the effects of atmospheric stability and turbulence on the  
 121 wind profile [16]. By the ABL method suggested by Richards and Hoxey  
 122 [17], the flow velocity  $\vec{u} = (u, v)$  is calibrated to  $\vec{u}_{ABL} = (u_{ABL}, v_{ABL})$  by

$$\vec{u}_{ABL}(y) = \vec{u}_{ref} \frac{\ln\left(\frac{y_{ref}+y_0}{y_0}\right)}{\ln\left(\frac{y+y_0}{y_0}\right)}, \quad (1)$$

123 where  $y$  is the height of the wind field to be converted,  $y_0 = 0.0002$  is  
 124 the aerodynamic roughness length at sea level,  $\vec{u}_{ABL}^*$  is the ABL friction



125 velocity,  $y_{ref}$  is set to  $50m$ , and  $\vec{u}_{ref}$  is the wind velocity at an altitude of  
 126  $50m$ . Using the ABL calibration, prediction and training of wind velocity  
 127 at an altitude of  $100m$  is demonstrated in this study.

128 After performing ABL calibration, the calibrated wind velocity ( $u_{ABL}$   
 129 and  $v_{ABL}$ ) is further standardized as

$$u_{std} = \frac{u_{ABL} - \mu_{u_{ABL}}}{\sigma_{u_{ABL}}} \quad (2)$$

130 and

$$v_{std} = \frac{v_{ABL} - \mu_{v_{ABL}}}{\sigma_{v_{ABL}}} \quad (3)$$

131 where  $u_{std}$  and  $v_{std}$  are the standardized velocity components,  $\mu_{u_{ABL}}$  and  
 132  $\mu_{v_{ABL}}$  are the mean of the velocity components, and  $\sigma_{u_{ABL}}$  and  $\sigma_{v_{ABL}}$  are  
 133 the standard deviations of the velocity components. This standardization  
 134 ensures that all features have similar scales and distributions.

### 135 3.2. Neural network model

136 Neural networks have shown promising results in solving nonlinear prob-  
 137 lems and have been increasingly used in wind power research [18, 19, 20,  
 138 21, 22, 23]. In this study, a 2D+3D-CNN architecture based on the model  
 139 proposed by Higashiyama et al. [13] was employed. The CNN is designed to  
 140 learn spatiotemporal hierarchies of features in data by adjusting the weights  
 141 and biases of convolutional filters. 3D convolutional filters move in three  
 142 directions: 2D in space and 1D in time. A schematic of the 2D+3D-CNN  
 143 model used in this paper can be seen in Figure4. This model employs the  
 144 He uniform variance scaling initializer [24] for weights and biases of 2D and  
 145 3D convolutional filters, which is commonly used to facilitate more effec-  
 146 tive training of neural networks with Rectified Linear Unit (ReLU)-type  
 147 activation functions. The range of the initial weights and biases is defined  
 148 as

$$\left(-\sqrt{\frac{6}{n_{in}}}, \sqrt{\frac{6}{n_{in}}}\right), \quad (4)$$

149  $n_{in}$  represents the number of feature maps or nodes in the layer to be ini-  
 150 tialized. The leaky-ReLU activation function, a variation of the ReLU ac-  
 151 tivation function [25], was employed. Leaky-ReLU is defined as

$$f(x) = \max(\alpha x, x), \quad (5)$$

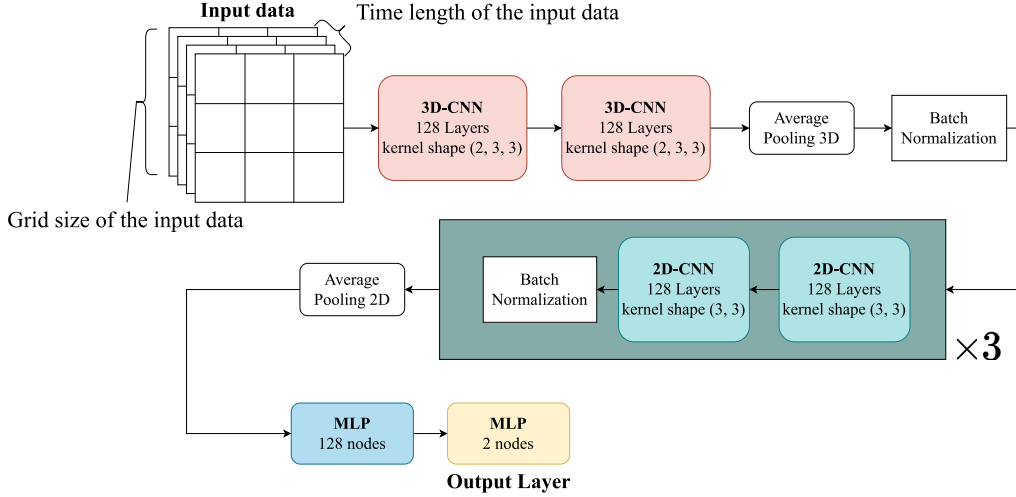


Figure 4: Schematic of the 3D-CNN model used in this study.

152 where  $x$  is an arbitrary tensor and  $\alpha = 0.3$  was used in this study.

153 The Adaptive Moment Estimation (Adam) optimizer [26], known for its  
 154 efficient computational properties, its adaptive learning rate per parame-  
 155 ter, and its use of both the first and second moments of the gradient, was  
 156 used to train the model. Also, the model is trained to minimize the Hu-  
 157 ber loss [27]. This loss function is less sensitive to the presence of outliers  
 158 in the training data, making it a more reliable measure of a model's per-  
 159 formance in real-world scenarios. The Huber loss function is commonly  
 160 employed in regression problems because it offers a balance between the  
 161 mean squared error (MSE) and mean absolute error (MAE) loss functions,  
 162 enabling it to handle both small and large deviations between the predicted  
 163 and ground-truth values. In addition, batch normalization layers are used  
 164 to reduce overfitting and increase learning stability by shifting the layer in-  
 165 puts to zero mean and unit variance [28]. All neural network models used  
 166 in this paper were implemented using Python 3.10.6 and Keras [29]. Ad-  
 167 ditionally, the models were trained using two NVIDIA GeForce RTX 3060  
 168 graphics processing units (GPU).

## 169 4. Results

170 The coefficient of determination  $R^2$  is used to evaluate the prediction  
 171 performance and is defined as

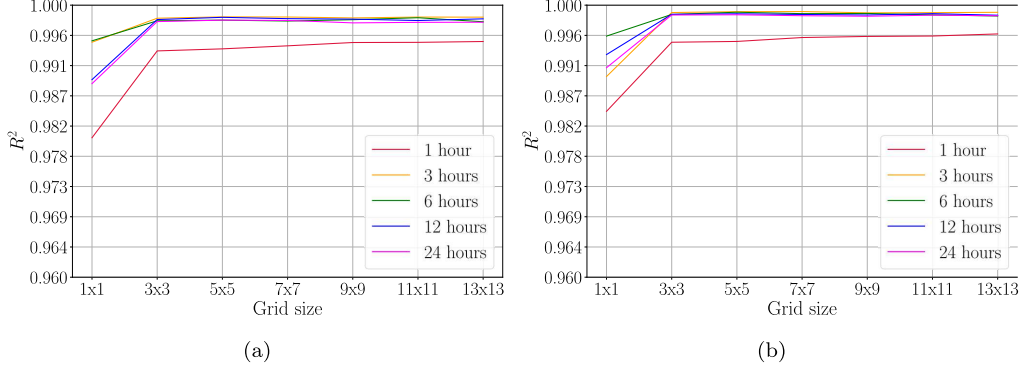


Figure 5: Variations in  $R^2$  values for predicting  $u$  (a) and  $v$  (b) with changing grid sizes and input time lengths in Korea.

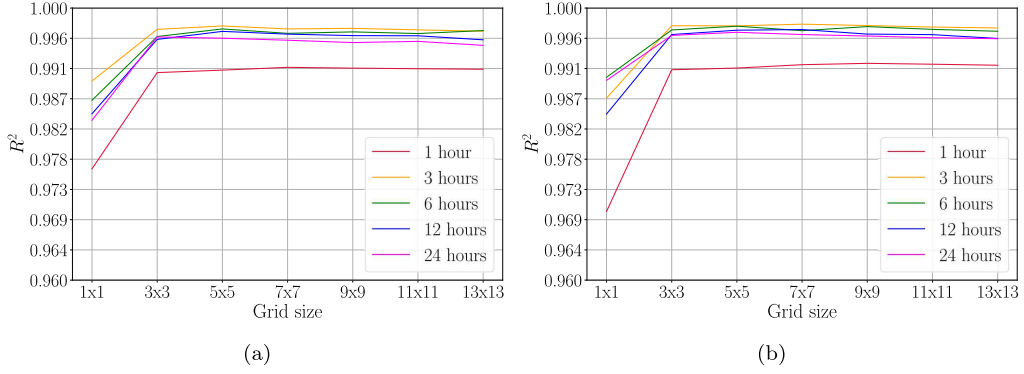


Figure 6: Variations in  $R^2$  values for predicting  $u$  (a) and  $v$  (b) with changing grid sizes and input time lengths in the USA.

$$R^2 = \frac{\sum_{i=1}^n (\hat{y}_i - \bar{y})^2}{\sum_{i=1}^n (y_i - \bar{y})^2}, \quad (6)$$

172 where  $y_i$  is the ground truth value,  $\bar{y}$  is the mean of the ground truth values  
 173 and  $\hat{y}_i$  is the predicted value. The value of  $R^2$  ranges from 0 to 1, with a  
 174 value closer to 1 indicating a more accurate model and a value closer to 0  
 175 indicating a less accurate model.

176 The evaluation of the prediction performance with respect to the change  
 177 in the spatiotemporal size of the input data is presented in Figures 5–7 and  
 178 Tables 2–4. Each color represents a different time length for the input

$u$	$1 \times 1$	$3 \times 3$	$5 \times 5$	$7 \times 7$	$9 \times 9$	$11 \times 11$	$13 \times 13$
<b>1</b>	0.970	0.983	0.986	0.987	0.986	0.986	0.986
<b>3</b>	0.992	0.995	0.996	0.996	0.996	0.995	0.996
<b>6</b>	0.989	0.995	0.996	0.996	0.995	0.994	0.995
<b>12</b>	0.985	0.994	0.994	0.994	0.993	0.993	0.992
<b>24</b>	0.982	0.993	0.993	0.993	0.992	0.992	0.992

$v$	$1 \times 1$	$3 \times 3$	$5 \times 5$	$7 \times 7$	$9 \times 9$	$11 \times 11$	$13 \times 13$
<b>1</b>	0.968	0.987	0.988	0.989	0.989	0.988	0.989
<b>3</b>	0.992	0.996	0.997	0.996	0.996	0.996	0.996
<b>6</b>	0.989	0.996	0.996	0.996	0.995	0.995	0.995
<b>12</b>	0.985	0.995	0.994	0.995	0.994	0.993	0.993
<b>24</b>	0.982	0.994	0.994	0.994	0.993	0.993	0.992

Table 2:  $R^2$  values for predicting  $u$ ,  $v$  with changing grid sizes and input time lengths in Korea.

$u$	$1 \times 1$	$3 \times 3$	$5 \times 5$	$7 \times 7$	$9 \times 9$	$11 \times 11$	$13 \times 13$
<b>1</b>	0.976	0.991	0.991	0.991	0.991	0.991	0.991
<b>3</b>	0.989	0.997	0.997	0.997	0.997	0.997	0.997
<b>6</b>	0.986	0.996	0.997	0.996	0.996	0.996	0.997
<b>12</b>	0.984	0.995	0.997	0.996	0.996	0.996	0.995
<b>24</b>	0.984	0.996	0.996	0.995	0.995	0.995	0.995

$v$	$1 \times 1$	$3 \times 3$	$5 \times 5$	$7 \times 7$	$9 \times 9$	$11 \times 11$	$13 \times 13$
<b>1</b>	0.970	0.991	0.991	0.992	0.992	0.992	0.992
<b>3</b>	0.987	0.997	0.997	0.998	0.997	0.997	0.997
<b>6</b>	0.990	0.997	0.997	0.997	0.997	0.997	0.997
<b>12</b>	0.984	0.996	0.997	0.997	0.996	0.996	0.996
<b>24</b>	0.989	0.996	0.996	0.996	0.996	0.996	0.995

Table 3:  $R^2$  values for predicting  $u$ ,  $v$  with changing grid sizes and input time lengths in the USA.

179 data. In terms of spatial aspects, providing additional surrounding data  
180 to the 2D+3D-CNN model improved the prediction accuracy compared to  
181 providing a single space ( $1 \times 1$ ), regardless of the time length. However, no  
182 significant difference was observed in the values of  $R^2$  when the spatial area  
183 was increased by more than  $3 \times 3$ .

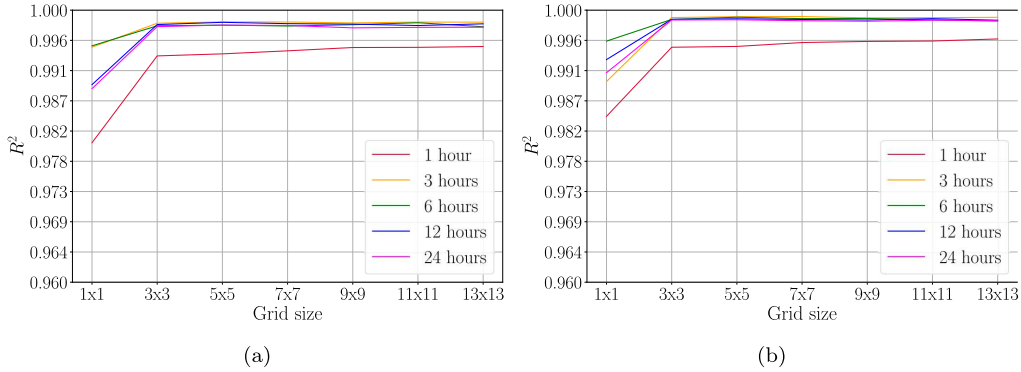


Figure 7: Variations in  $R^2$  values for predicting  $u$  (a) and  $v$  (b) with changing grid sizes and input time lengths in the UK.

$u$	$1 \times 1$	$3 \times 3$	$5 \times 5$	$7 \times 7$	$9 \times 9$	$11 \times 11$	$13 \times 13$
<b>1</b>	0.981	0.993	0.994	0.994	0.995	0.995	0.995
<b>3</b>	0.995	0.998	0.998	0.998	0.998	0.998	0.998
<b>6</b>	0.995	0.998	0.998	0.998	0.998	0.998	0.998
<b>12</b>	0.989	0.998	0.998	0.998	0.998	0.998	0.998
<b>24</b>	0.988	0.998	0.998	0.998	0.997	0.997	0.997

$v$	$1 \times 1$	$3 \times 3$	$5 \times 5$	$7 \times 7$	$9 \times 9$	$11 \times 11$	$13 \times 13$
<b>1</b>	0.984	0.995	0.995	0.995	0.995	0.995	0.996
<b>3</b>	0.990	0.999	0.999	0.999	0.999	0.999	0.999
<b>6</b>	0.995	0.999	0.999	0.999	0.999	0.999	0.998
<b>12</b>	0.993	0.999	0.999	0.999	0.999	0.999	0.999
<b>24</b>	0.991	0.999	0.999	0.998	0.998	0.999	0.998

Table 4:  $R^2$  values for predicting  $u$ ,  $v$  with changing grid sizes and input time lengths in the UK.

184 Similarly, in terms of the time length, using a single time step resulted in  
 185 the worst prediction performance in every case. The lower accuracy achieved  
 186 with a single-time-step input can be attributed to the inherent limitations  
 187 in capturing temporal trends with only a single snapshot. Overall, the best  
 188 predictions were obtained at a time of 3 hours. No significant difference was  
 189 observed in the values of  $R^2$  between the 3 h and 24 h time periods.

190 In contrast, the impact of regional differences on observed variations is  
 191 noteworthy. Figure 8 provides a clear visualization of the regional discrep-

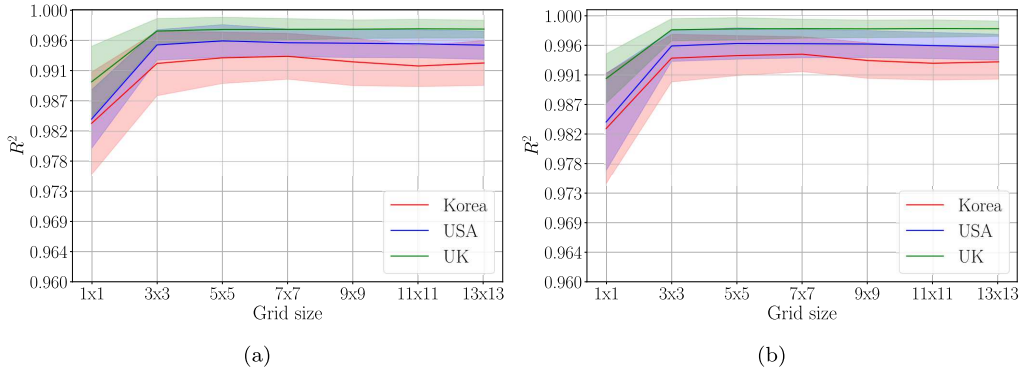


Figure 8: Comparison of  $R^2$  with varying spatial input data for predicting  $u$  (a) and  $v$  (b). The solid lines represent the average  $R^2$  values across all time lengths, and the shaded area indicates the range of minimum and maximum  $R^2$  values.

192 ancies in predicting  $u$  and  $v$ . Korea has the highest variance in  $R^2$  compared  
 193 to the USA and UK. In addition, Korea has the lowest average  $R^2$  value for  
 194 all grid sizes.

195 To investigate the cause of the performance differences resulting from  
 196 the different temporal flow scales in the tested regions, an autocorrelation  
 197 analysis was employed. Autocorrelation measures the linear relationship  
 198 between time-series data and their shifted versions. A low autocorrelation  
 199 coefficient (ACC) indicates a weak correlation between the original data and  
 200 the same data shifted by a certain time lag, whereas a high ACC suggests  
 201 a strong correlation between the original and shifted data. ACC can be  
 202 calculated as

$$r_k = \frac{\sum_{t=k+1}^n (y_t - \bar{y})(y_{t-k} - \bar{y})}{\sum_{t=1}^n (y_t - \bar{y})^2}, \quad (7)$$

203 where  $r_k$  represents the ACC at lag  $k$ ,  $y_t$  is the value of the time series at  
 204 time  $t$ , and  $n$  is the total number of time steps.  $\bar{y}$  represents the mean of  
 205 the time series.

206 Figure 9 shows the ACC values for the  $13 \times 13$  grid space. As shown  
 207 in the figure, the ACC values for all three regions steadily decreased as  
 208 the time lag increased. However, the rate of decrease varied across regions,  
 209 with the ACC of the UK displaying the gentlest slope, whereas those of  
 210 Korea and the USA exhibited steeper slopes. This trend aligns with the

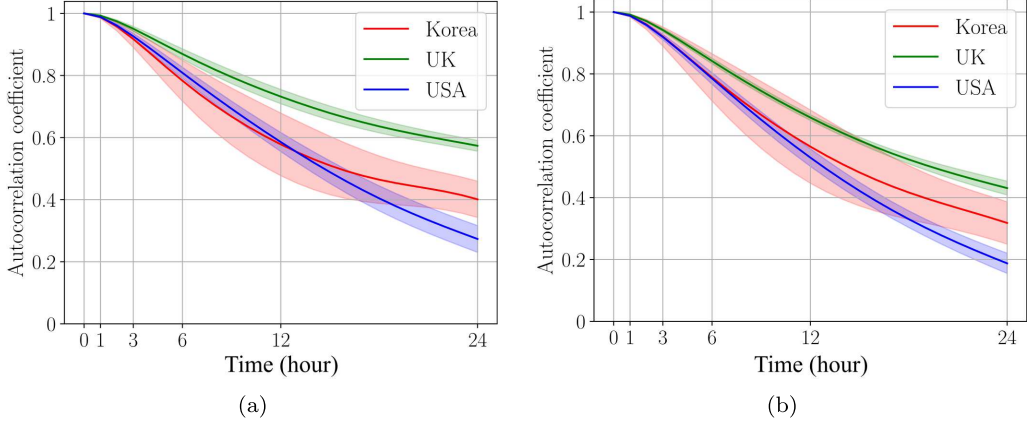


Figure 9: ACCs of (a)  $u$  and (b)  $v$ . The y-axis represents the ACC values, while the x-axis represents the input time lengths. The solid line indicates the mean value, and the shaded area stands for the minimum and maximum ACC values.

211 observations in Figure 10 and Table 6, which highlight a larger change in  
 212  $R^2$  with changing input time lengths in Korea and the USA compared to  
 213 the UK.

214 Furthermore, it is worth noting that the shaded areas in Figure 9 vary  
 215 across different regions. These shaded areas are represented based on the  
 216 standard deviation calculated as

$$\sigma_k = \sqrt{\frac{\sum_{i=1}^n (r_{k,i} - \mu_k)^2}{n}}, \quad (8)$$

217 where  $\sigma_k$  is the standard deviation of ACC values at time lag  $k$ ,  $r_{k,i}$  is the  
 218 ACC value at time lag  $k$  and  $i$ -th location in the grid space,  $\mu_k$  is the spatial  
 219 average of  $r_{k,i}$ , and  $n$  is the total number of spatial grid points. Furthermore,  
 220 the maximum standard deviations across different regions over time were  
 221 calculated as  $\max_k(\sigma_k)$ . These results are presented in Table 5. The regions  
 222 with the highest maximum standard deviations were found to be in the  
 223 following order: Korea, USA, and UK; while the predictive performances  
 224 ( $R^2$ ) were observed to be the best in the reverse order: UK, USA, and  
 225 Korea. This result indicates that a CNN's learnability is highly dependent  
 226 on regional spatiotemporal wind characteristics that could be quantified by  
 227 calculating ACCs.

228 To further investigate the spatial effect, a Pearson correlation coefficient  
 229 (PCC) analysis was conducted. PCC is a statistical tool used to quantify  
 230 the linear correlation between variables. The PCC of the two variables,  $a$   
 231 and  $b$ , is defined by

	<b>Korea</b>	<b>USA</b>	<b>UK</b>
$u$	0.101	0.043	0.023
$v$	0.119	0.033	0.022

Table 5: The maximum standard deviation of ACC of  $u, v$  values for each region.

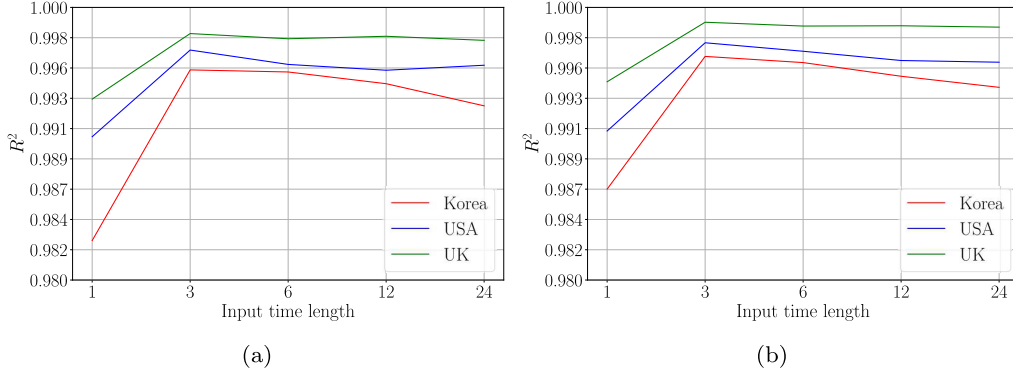


Figure 10: Effect of increasing input time length on performance ( $R^2$ ) with a fixed grid size of  $3 \times 3$  for  $u$  (a) and  $v$  (b).

$u$	<b>1</b>	<b>3</b>	<b>6</b>	<b>12</b>	<b>24</b>
<b>Korea</b>	0.983	0.995	0.995	0.994	0.993
<b>USA</b>	0.991	0.997	0.996	0.995	0.996
<b>UK</b>	0.993	0.998	0.998	0.998	0.998

$v$	<b>1</b>	<b>3</b>	<b>6</b>	<b>12</b>	<b>24</b>
<b>Korea</b>	0.987	0.996	0.996	0.995	0.994
<b>USA</b>	0.991	0.997	0.997	0.996	0.996
<b>UK</b>	0.995	0.999	0.999	0.999	0.999

Table 6: Effect of increasing input time length on performance ( $R^2$ ) with a fixed grid size of  $3 \times 3$  for  $u, v$

$$PCC = \frac{\sum_{i=1}^n (a_i - \bar{a})(b_i - \bar{b})}{\sqrt{\sum_{i=1}^n (a_i - \bar{a})^2} \sqrt{\sum_{i=1}^n (b_i - \bar{b})^2}}, \quad (9)$$

232 where  $\bar{a}$  and  $\bar{b}$  indicate the mean values of  $a$  and  $b$ , and  $n$  denotes the number  
233 of data points.



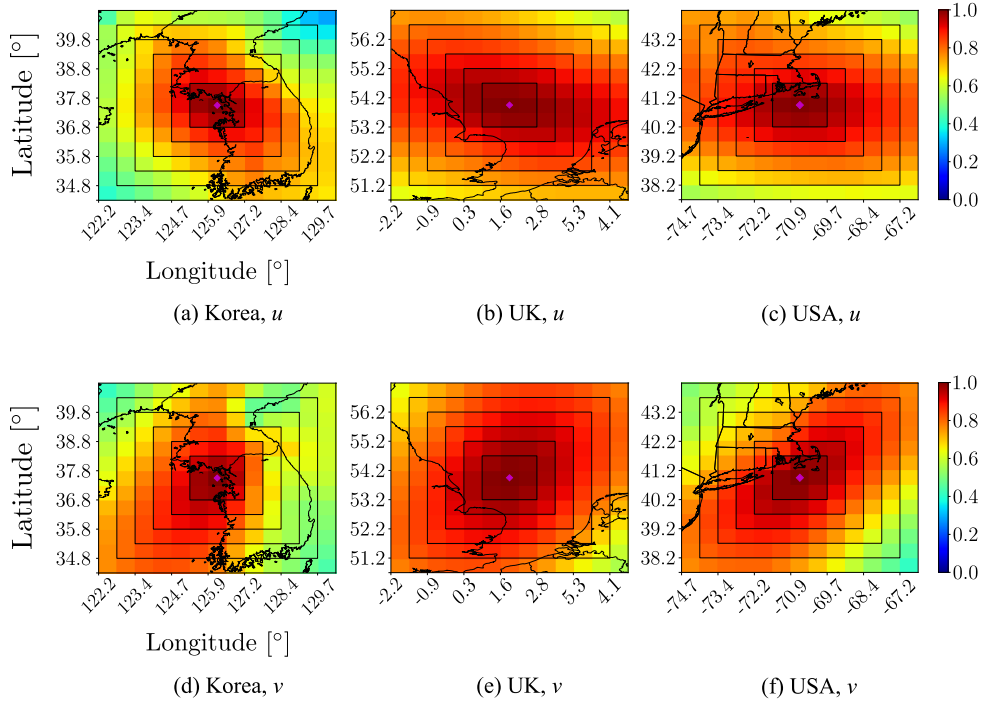


Figure 11: The PCC heatmaps of variable  $u$  across three regions over a 10-year period are depicted in (a) to (c), while the PCC heatmaps of variable  $v$  during the same period in these regions are shown in (d) to (f).

234 The variation in the PCC with respect to spatial size was examined to  
 235 determine the cause of the difference in forecasting performance by region.  
 236 Ten years of wind data were used to compute the PCC of both  $u$  and  $v$  at  
 237 each grid point and prediction point. The results are presented in the form  
 238 of heatmaps (Figure 11). The heatmaps revealed that the PCC values for  
 239 all three locations were similar up to a grid size of  $3 \times 3$ . For grid sizes  
 240 of  $5 \times 5$  and larger, the PCC values in Korea were lower than those in  
 241 the UK and USA for both velocity components. Among the three regions,  
 242 the UK exhibited the highest concentration of high PCC values. Figure 12  
 243 shows the average values of PCC with respect to grid size for each region,  
 244 excluding the prediction point. The UK displayed the smallest change in  
 245 the average  $u$  and  $v$  PCC.

246 The observed differences in PCC values across the three regions can be  
 247 attributed to their respective seasonal wind patterns. A closer look at the  
 248 wind fields in Korea, the USA, and the UK, as depicted in Figures 13, 14,  
 249 and 15, highlights that Korea exhibits the most intricate and complex wind

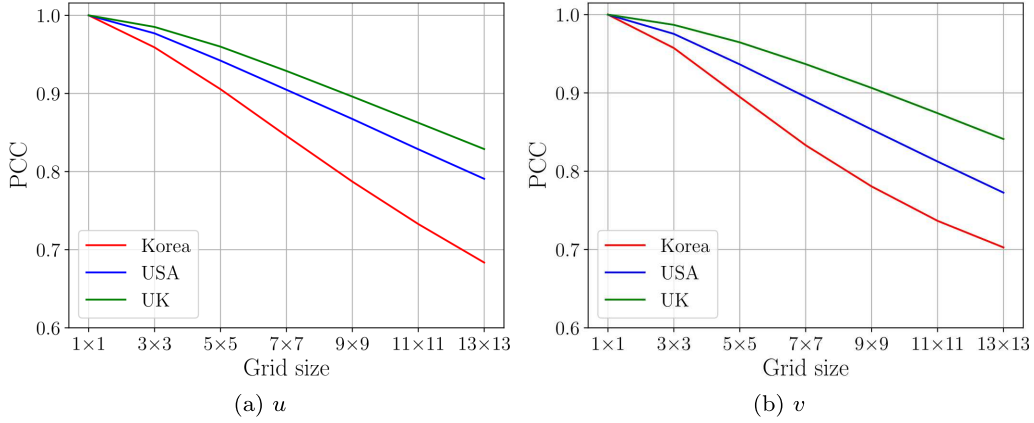


Figure 12: Changes in average PCC for (a)  $u$  and (b)  $v$  as grid size increases.

250 flow patterns unique to the region. During the winter, Korea is influenced by  
 251 northwest monsoons from Siberia, as shown in Figure 13 (d), whereas during  
 252 the summer, it is influenced by southeast monsoons from the North Pacific,  
 253 as shown in Figure 13 (b). Moreover, the complex terrain of Korea, with  
 254 its many mountains, greatly affects the flow of the near-surface atmosphere,  
 255 contributing to intricate wind patterns. In addition, Korea is affected by  
 256 strong tropical cyclones, known as typhoons, during the summer and fall,  
 257 further increasing the variability in wind patterns [30].

258 In contrast, the PCC values in the UK and the USA showed a more  
 259 even distribution with higher overall values. This can be attributed to  
 260 the topographic and meteorological features of these regions. The UK, in  
 261 particular, has a more gentle and flatter terrain than Korea, which does  
 262 not significantly impede the wind flow in the region. The prevailing winds  
 263 in this region are westerlies that blow from the Atlantic Ocean and are  
 264 relatively consistent throughout the year.

265 Similarly, the prevailing winds in the northeastern region of the US blow-  
 266 ing from the Pacific Ocean are westerlies. During the winter, the Northeast-  
 267 ern USA can experience extreme weather conditions due to the influence of  
 268 the “Polar Vortex” [31]. However, compared to the wind patterns in Korea,  
 269 the wind patterns in both the Northeastern UK and the USA are relatively  
 270 consistent throughout the year, which is reflected by a more even distribu-  
 271 tion of PCC values in these regions.

272 A comparative analysis was conducted to compare the predictive capa-  
 273 bility of the 2D+3D-CNN model employed in this research against state-of-  
 274 the-art wind prediction CNN models. Zhu et al. [14] introduced a Fully 3D-

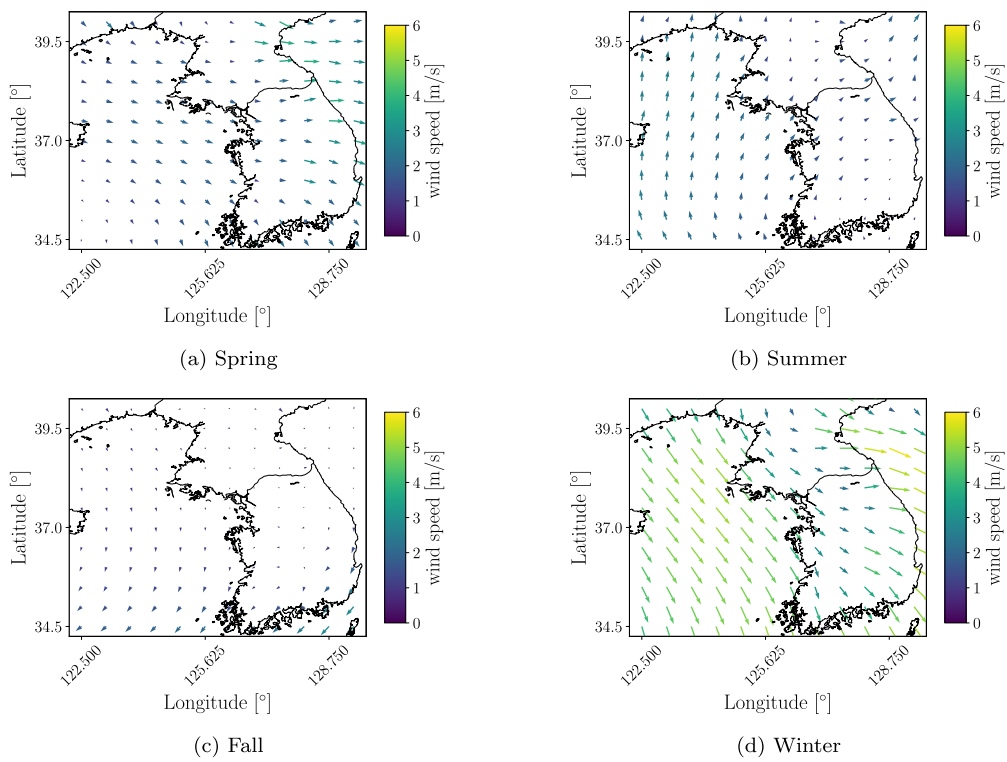


Figure 13: Wind field variations in Korea in four distinct seasons. The size of the arrow is proportional to the speed.

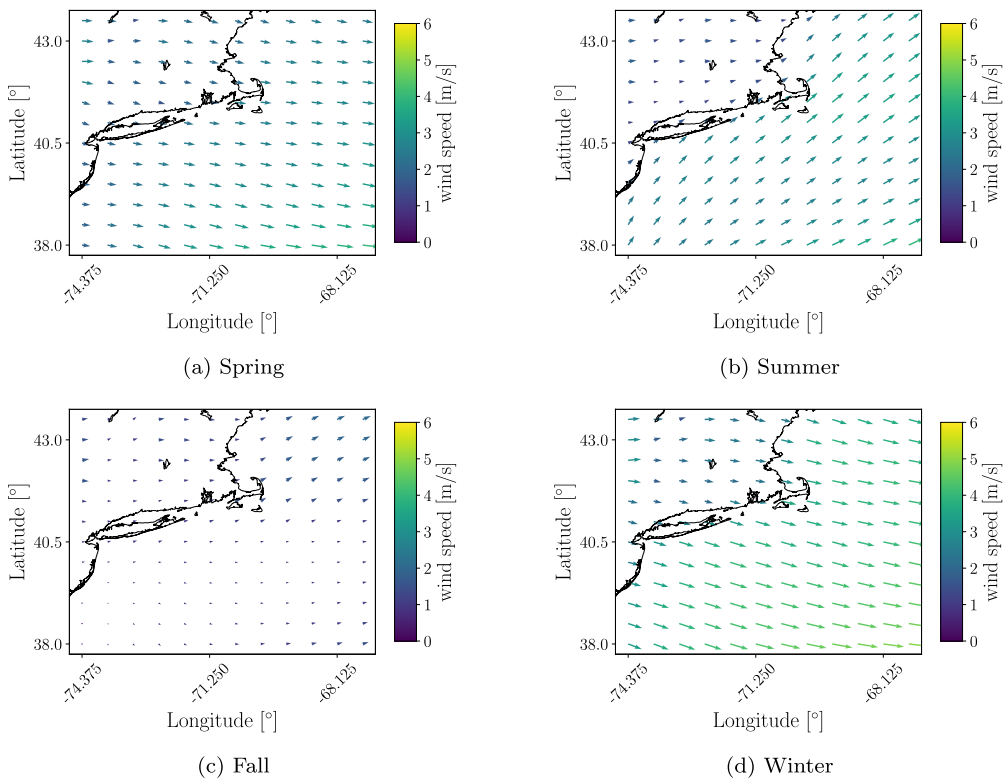


Figure 14: Wind field variations in the USA in four distinct seasons. The size of the arrow is proportional to the speed.

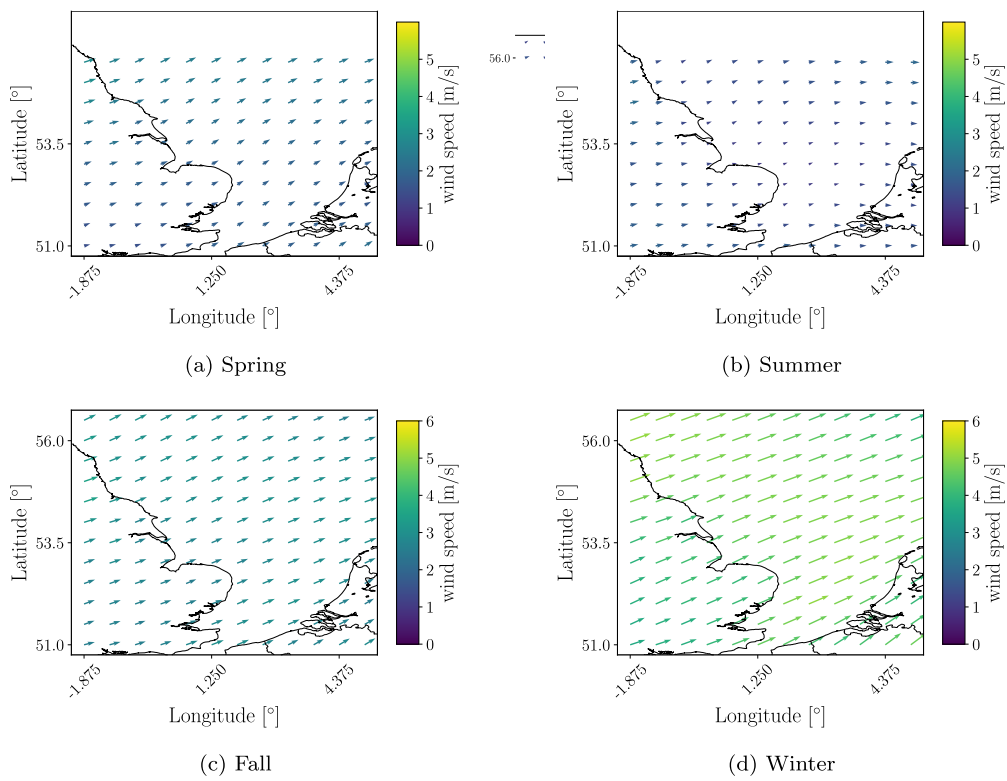


Figure 15: Wind field variations in the UK in four distinct seasons. The size of the arrow is proportional to the speed.

275 CNN model to capture spatiotemporal information, which is similar to the  
276 proposed 2D+3D-CNN model. The main distinction between the Fully 3D-  
277 CNN model and the current 2D+3D-CNN model is that the Fully 3D-CNN  
278 model does not include 2D-CNN layers. Shen et al. [32] employed a 1D-  
279 CNN model consisting of long short-term memory (LSTM) layers [33, 34],  
280 known for its ability to learn long-term dependencies in sequential data, to  
281 predict wind speeds for unmanned sailboat control systems.

282 The comparison was conducted using data with grid sizes ranging from  
283  $7 \times 7$  to  $13 \times 13$  and input time lengths of 6, 12, and 24, due to structural  
284 constraints in the models of the aforementioned studies. In this study,  
285 the last fully connected layer of the Fully 3D-CNN model, which originally  
286 consisted of seven neurons, was modified to have two neurons for predicting  
287  $u$  and  $v$  at future time steps. Similarly, the 1D-CNN was adjusted to include  
288 two cells in the last LSTM layer.

289 The predictive performances ( $R^2$ ) of the 1D-CNN and Fully 3D-CNN  
290 models were analyzed by varying the grid and time step sizes, as shown in  
291 Figures 16 and 17, respectively. The 1D-CNN model demonstrated similar  
292 performance even when using a longer history of time for wind prediction.  
293 In addition, the performance decreased when larger spatial information was  
294 included for training. Similarly, the Fully 3D-CNN model tended to show a  
295 performance drop when larger spatial data was included in the input. This  
296 observation was also consistent with the findings from the 2D+3D-CNN  
297 model when data with smaller spatiotemporal correlations (i.e., spatial data  
298 larger than  $7 \times 7$ ) were provided (Figure 8).

299 Overall, the present 2D+3D-CNN model demonstrates a significant per-  
300 formance improvement compared to the Fully 3D-CNN and 1D-CNN mod-  
301 els (Figure 18). This improvement can be attributed to the deep layers  
302 employed in the present 2D+3D-CNN model, which allows for efficient  
303 spatiotemporal feature extraction by utilizing both 2D and 3D convolu-  
304 tional layers. However, it is important to note that the 2D+3D-CNN model  
305 is specifically designed for spatiotemporal data with uniform resolutions  
306 in both space and time, whereas the 1D-CNN and Fully 3D-CNN mod-  
307 els were developed using real-world measurement data that are spatially  
308 sparse [14, 32]. As a result, the superior performance of the current model  
309 may not be guaranteed when applied to spatially sparse data.

310 Nevertheless, it is worth noting that all of the tested CNN models ex-  
311 hibit the best predictive performance in the order of regions in the UK, the  
312 USA, and Korea (Figures 8, 16, 17, and 18). This result suggests that

313 regional wind characteristics have a substantial impact on the performance  
314 of the predictive CNN models. Moreover, the regional wind effects on the  
315 neural network’s learnability can be estimated prior to training through the  
316 spatiotemporal correlation analysis proposed in this study.

## 317 5. Conclusions

318 This paper investigates how the performance of wind prediction CNN  
319 models can be influenced by regional wind characteristics. The proposed  
320 2D+3D CNN model is trained using past wind data from the surrounding  
321 area of a wind farm, considering different time lengths. By analyzing the  
322 relationship between regional wind characteristics and the model’s perfor-  
323 mance, we study the influence of spatiotemporal features of input wind data  
324 on predictive performances of CNN models.

325 Autocorrelation and Pearson correlation analyses are conducted on re-  
326 gional and seasonal wind data. Firstly, the autocorrelation analysis reveals  
327 that CNN predictive performances tend to decrease in regions with higher  
328 maximum standard deviations of the ACC across different regions. Notably,  
329 the regions with the highest maximum standard deviations are found to be  
330 in the following order: Korea, USA, and UK; while the predictive perfor-  
331 mances are observed to be the best in the reverse order: UK, USA, and  
332 Korea.

333 Secondly, Pearson correlation analysis is conducted to examine the spa-  
334 tial relationships within the data. Many low PCC values are observed in  
335 Korea, which align with the findings from the ACC analysis. The predictive  
336 performance of the CNN model increases when wind data from surrounding  
337 areas with high PCC values are included, while data from areas with low  
338 PCC values negatively impact the prediction performance. The variations  
339 in PCC value distribution among regions are attributed to meteorological  
340 and geographical factors, with Korea experiencing the most complex wind  
341 flow among the three regions due to these factors. Additionally, when train-  
342 ing different CNN models (2D+3D-CNN model, Fully 3D-CNN model, and  
343 1D-CNN model), it is observed that all of the CNN models exhibit a de-  
344 crease in predictive performance when the spatiotemporal correlations of  
345 the regional wind are reduced.

346 In conclusion, incorporating favorably correlated spatial and temporal  
347 wind data from surrounding areas improves the predictive performances of  
348 CNN models. It is worth noting that the correlation analysis is a pure  
349 data analysis and does not involve training a CNN. Therefore, the proposed

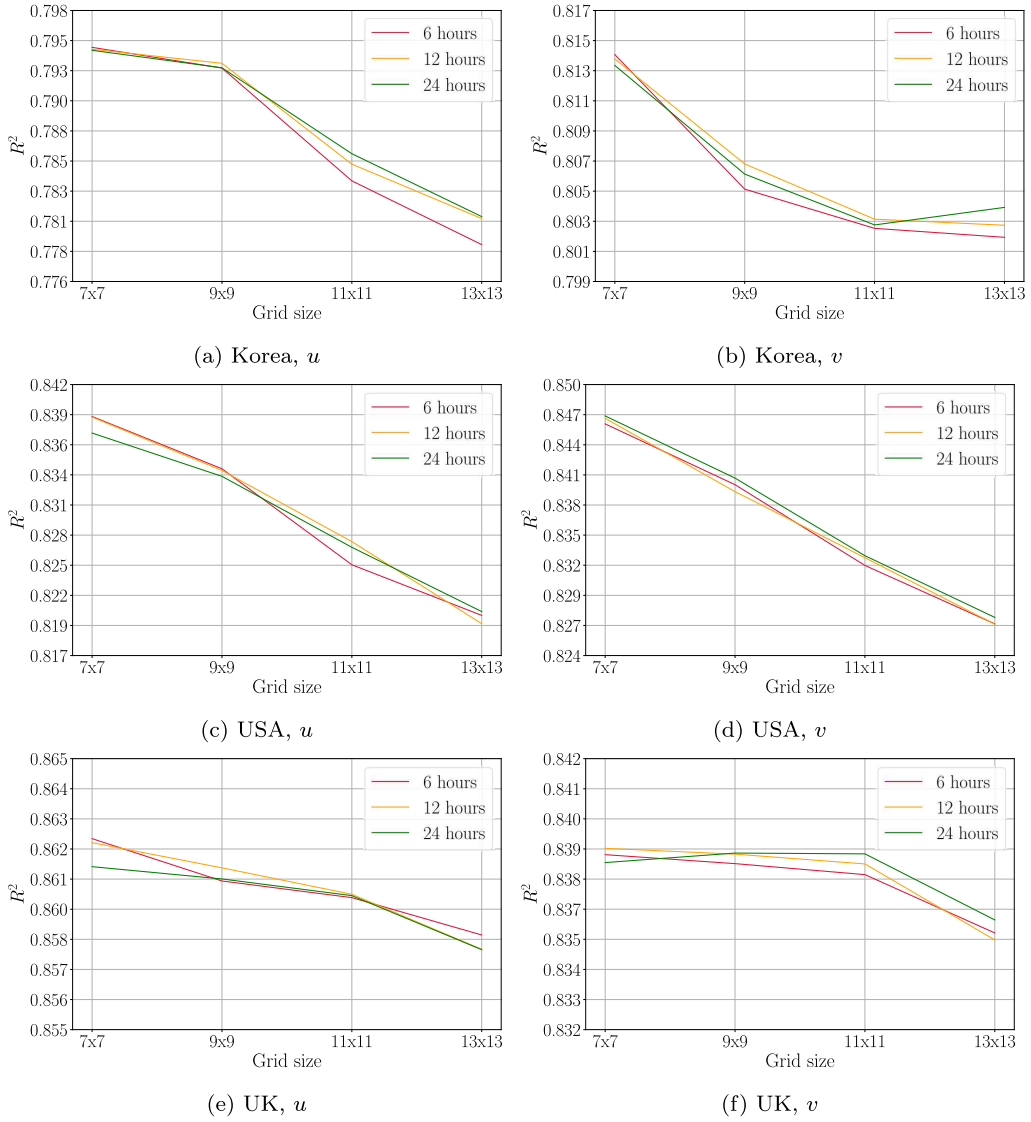


Figure 16: Variations in  $R^2$  values for predicting  $u$  and  $v$  with changing grid sizes and input time lengths using the 1D-CNN model in Korea, USA, and UK.



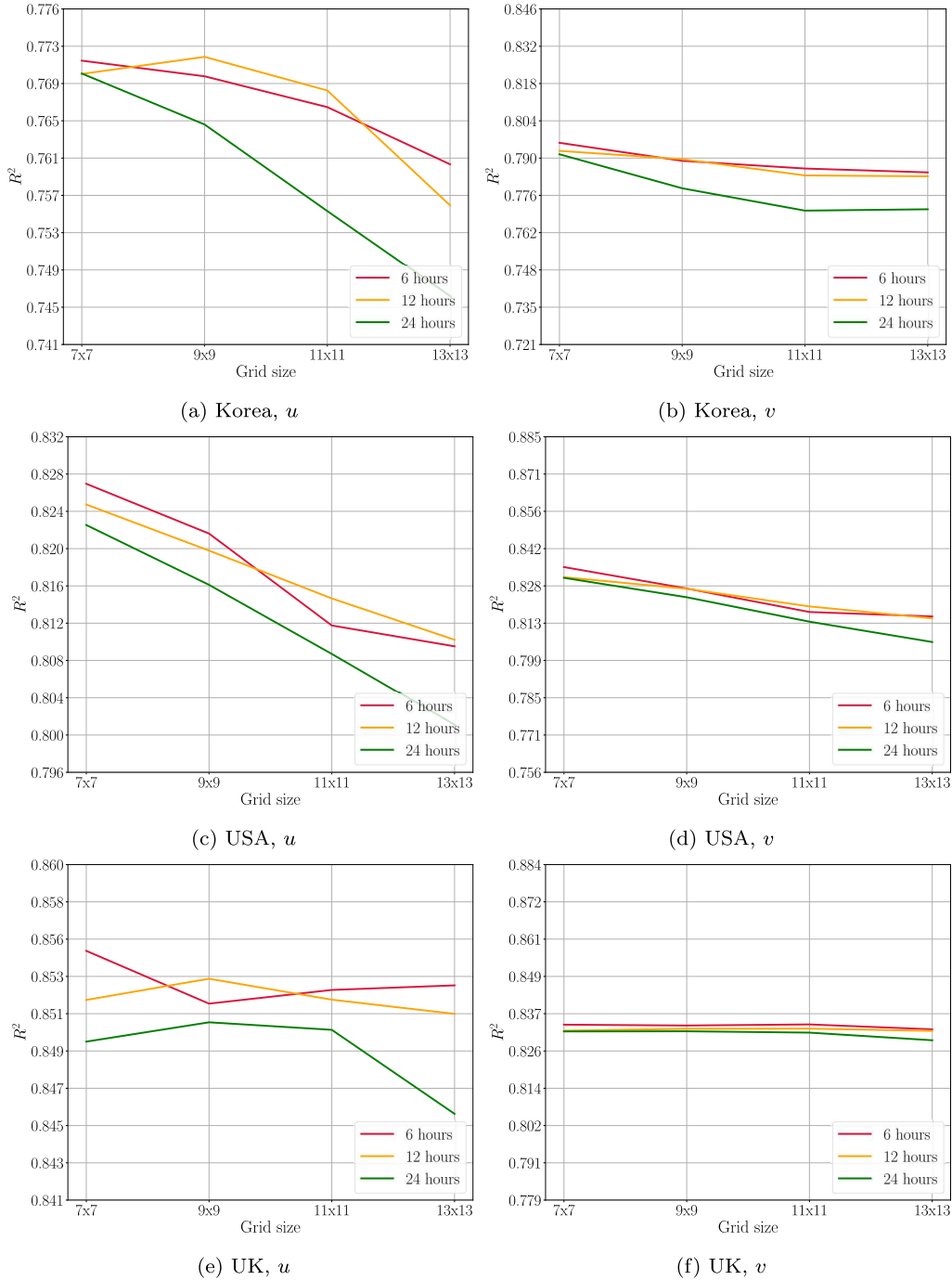


Figure 17: Variations in  $R^2$  values for predicting  $u$  and  $v$  with changing grid sizes and input time lengths using the fully 3D-CNN model in Korea, USA, and UK.

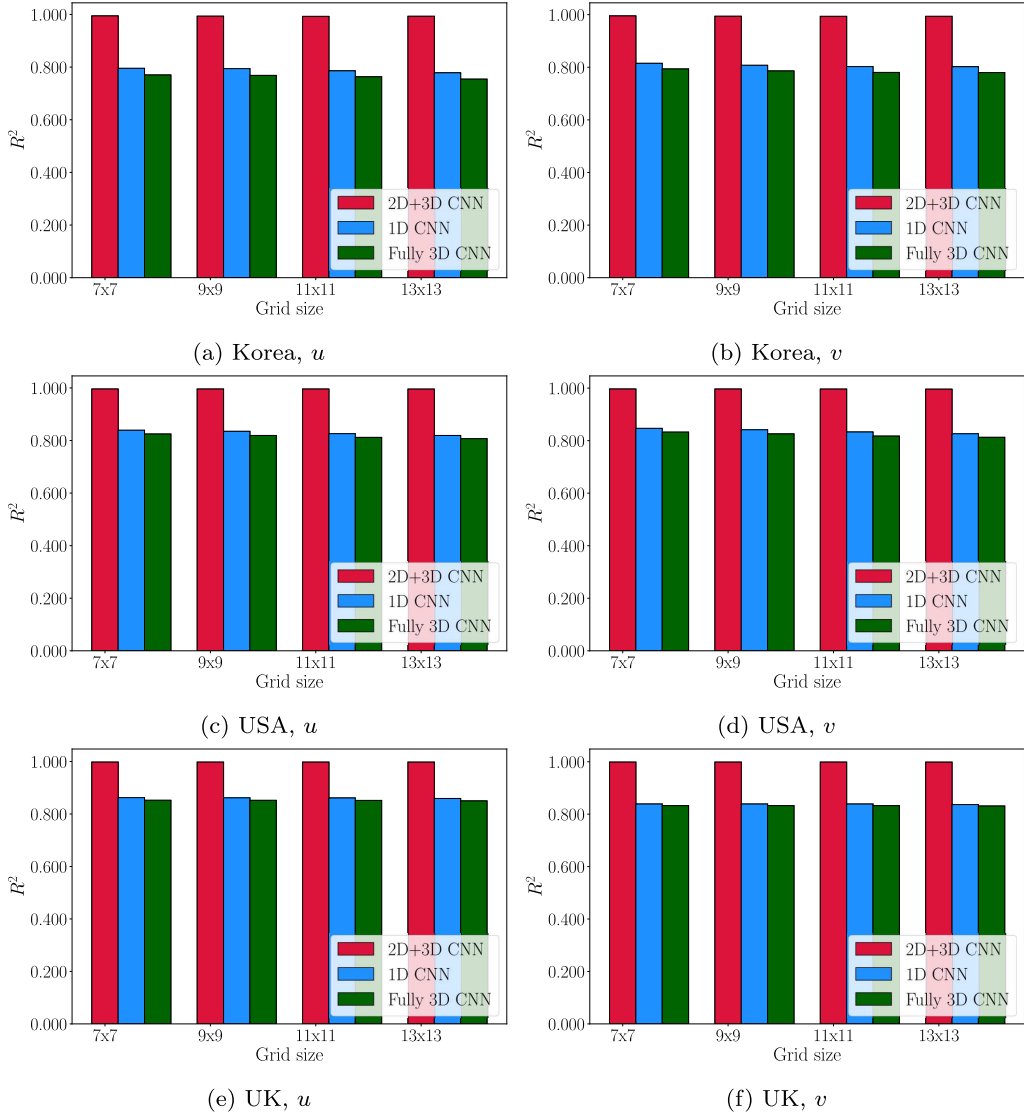


Figure 18: Comparison of average  $R^2$  in predicting (a)  $u$  and (b)  $v$  between models by grid size in Korea, USA, and UK. The models by Zhu et al. [14], Shen et al. [32], and the current study are represented in the figure as Fully 3D CNN, 1D CNN, and 2D+3D CNN, respectively.

350 correlation analyses can be employed to estimate the learnability of a CNN  
351 prior to the training process. In addition, based on the findings in this  
352 study, it is recommended that wind turbines be installed in areas with high  
353 PCC values and small maximum standard deviations of ACCs to enable  
354 efficient power generation using CNN-based prediction/control methods.

## 355 **Acknowledgements**

356 This work was supported by the National Research Foundation of Ko-  
357 rea Grant funded by the Korean Government (NRF-2022R1F1A1066547);  
358 INHA UNIVERSITY Research Grant (2023). MR acknowledges the CoE  
359 RAISE project, which receives funding from the European Union’s Horizon  
360 2020 –Research and Innovation Framework Programme H2020-INFRAEDI-  
361 2019-1 under grant agreement no. 951733. This work was performed as part  
362 of the Helmholtz School for Data Science in Life, Earth and Energy (HDS-  
363 LEE).

## **References**

- [1] F. Z. Joyce Lee, GLOBAL WIND REPORT 2022, Technical Report, Global Wind Energy Council, 2022.
- [2] J. Yang, L. Fang, D. Song, M. Su, X. Yang, L. Huang, Y. H. Joo, Review of control strategy of large horizontal-axis wind turbines yaw system, *Wind Energy* 24 (2021) 97–115.
- [3] D. Song, J. Yang, X. Fan, Y. Liu, A. Liu, G. Chen, Y. H. Joo, Maximum power extraction for wind turbines through a novel yaw control solution using predicted wind directions, *Energy conversion and management* 157 (2018) 587–599.
- [4] M. Kim, P. Dalhoff, Yaw systems for wind turbines—overview of concepts, current challenges and design methods, in: *Journal of Physics: Conference Series*, volume 524, IOP Publishing, 2014, p. 012086.
- [5] Y. Wang, R. Zou, F. Liu, L. Zhang, Q. Liu, A review of wind speed and wind power forecasting with deep neural networks, *Applied Energy* 304 (2021) 117766.
- [6] N. Hure, R. Turnar, M. Vašak, G. Benčić, Optimal wind turbine yaw control supported with very short-term wind predictions, in: *2015 IEEE International Conference on Industrial Technology (ICIT)*, IEEE, 2015, pp. 385–391.
- [7] M. Rüttgers, S. Lee, S. Jeon, D. You, Prediction of a typhoon track using a generative adversarial network and satellite images, *Scientific reports* 9 (2019) 1–15.
- [8] M. Rüttgers, S. Jeon, S. Lee, D. You, Prediction of typhoon track and intensity using a generative adversarial network with observational and meteorological data, *IEEE Access* 10 (2022) 48434–48446.
- [9] S. Harbola, V. Coors, One dimensional convolutional neural network architectures for wind prediction, *Energy Conversion and Management* 195 (2019) 70–75.

- [10] P. Ramasamy, S. Chandel, A. K. Yadav, Wind speed prediction in the mountainous region of india using an artificial neural network model, *Renewable Energy* 80 (2015) 338–347.
- [11] H. Jiajun, Y. Chuanjin, L. Yongle, X. Huoyue, Ultra-short term wind prediction with wavelet transform, deep belief network and ensemble learning, *Energy Conversion and Management* 205 (2020) 112418.
- [12] Y.-Y. Hong, T. R. A. Satriani, Day-ahead spatiotemporal wind speed forecasting using robust design-based deep learning neural network, *Energy* 209 (2020) 118441.
- [13] K. Higashiyama, Y. Fujimoto, Y. Hayashi, Feature extraction of NWP data for wind power forecasting using 3D-convolutional neural networks, *Energy Procedia* 155 (2018) 350–358.
- [14] X. Zhu, R. Liu, Y. Chen, X. Gao, Y. Wang, Z. Xu, Wind speed behaviors feather analysis and its utilization on wind speed prediction using 3D-CNN, *Energy* 236 (2021) 121523.
- [15] G. Modeling, A. O. (GMAO), MERRA-2 tavg1\_2d\_slv\_nx: 2d, 1hourly, time-averaged, singlelevel, assimilation, singlelevel diagnostics v5.12.4, greenbelt, MD, USA, goddard earth sciences data and information services center (ges disc), [https://disc.gsfc.nasa.gov/datasets/M2T1NXSLV\\_5.12.4/summary](https://disc.gsfc.nasa.gov/datasets/M2T1NXSLV_5.12.4/summary), 2015. [Online; accessed 16-September-2022].
- [16] B. Blocken, T. Stathopoulos, J. Carmeliet, CFD simulation of the atmospheric boundary layer: wall function problems, *Atmospheric environment* 41 (2007) 238–252.
- [17] P. Richards, R. Hoxey, Appropriate boundary conditions for computational wind engineering models using the k- $\epsilon$  turbulence model, *Journal of wind engineering and industrial aerodynamics* 46 (1993) 145–153.
- [18] H. Shin, M. Rüttgers, S. Lee, Neural networks for improving wind power efficiency: A review, *Fluids* 7 (2022) 367.
- [19] F. Shahid, A. Zameer, M. Muneeb, A novel genetic lstm model for wind power forecast, *Energy* 223 (2021) 120069.
- [20] R. Meka, A. Alaeddini, K. Bhaganagar, A robust deep learning framework for short-term wind power forecast of a full-scale wind farm using atmospheric variables, *Energy* 221 (2021) 119759.
- [21] J. E. Sierra-Garcia, M. Santos, Deep learning and fuzzy logic to implement a hybrid wind turbine pitch control, *Neural Computing and Applications* (2021) 1–15.
- [22] L. Jia, J. Hao, J. Hall, H. K. Nejadkhaki, G. Wang, Y. Yan, M. Sun, A reinforcement learning based blade twist angle distribution searching method for optimizing wind turbine energy power, *Energy* 215 (2021) 119148.
- [23] M. F. Howland, J. B. Quesada, J. J. P. Martínez, F. P. Larrañaga, N. Yadav, J. S. Chawla, V. Sivaram, J. O. Dabiri, Collective wind farm operation based on a predictive model increases utility-scale energy production, *Nature Energy* 7 (2022) 818–827.
- [24] K. He, X. Zhang, S. Ren, J. Sun, Delving deep into rectifiers: Surpassing human-level performance on imagenet classification, in: *Proceedings of the IEEE international conference on computer vision*, 2015, pp. 1026–1034.
- [25] A. Krizhevsky, I. Sutskever, G. E. Hinton, Imagenet classification with deep convolutional neural networks, *Communications of the ACM* 60 (2017) 84–90.

- [26] D. P. Kingma, J. Ba, Adam: A method for stochastic optimization, arXiv preprint arXiv:1412.6980 (2014).
- [27] P. J. Huber, Robust estimation of a location parameter, *Breakthroughs in statistics: Methodology and distribution* (1992) 492–518.
- [28] S. Ioffe, C. Szegedy, Batch normalization: Accelerating deep network training by reducing internal covariate shift, in: *International conference on machine learning*, pmlr, 2015, pp. 448–456.
- [29] F. Chollet, et al., Keras, <https://github.com/fchollet/keras>, 2015.
- [30] J.-Y. Kim, D.-Y. Kim, Spatio-temporal characteristics of wind observations over south korea: 1982–2011, *Asia-Pacific Journal of Atmospheric Sciences* 49 (2013) 551–560.
- [31] J. E. Overland, M. Wang, Impact of the winter polar vortex on greater north america, *International Journal of Climatology* 39 (2019) 5815–5821.
- [32] Z. Shen, X. Fan, L. Zhang, H. Yu, Wind speed prediction of unmanned sailboat based on cnn and lstm hybrid neural network, *Ocean Engineering* 254 (2022) 111352.
- [33] S. Hochreiter, J. Schmidhuber, Long short-term memory, *Neural computation* 9 (1997) 1735–1780.
- [34] K. Greff, R. K. Srivastava, J. Koutník, B. R. Steunebrink, J. Schmidhuber, Lstm: A search space odyssey, *IEEE transactions on neural networks and learning systems* 28 (2016) 2222–2232.